Flourishing ocean drives the end-Permian marine mass extinction

Martin Schobben[a,1], Alan Stebbins[b], Abbas Ghaderi[c], Harald Strauss[d], Dieter Korn[a], and Christoph Korte[e]

[a]Museum für Naturkunde, Leibniz-Institut für Evolutions- und Biodiversitätsforschung, D-10115 Berlin, Germany; [b]School for the Environment, University of Massachusetts Boston, Boston, MA 02125; [c]Department of Geology, Faculty of Sciences, Ferdowsi University of Mashhad, 9177948974 Mashhad, Iran; [d]Institut für Geologie und Paläontologie, Westfälische Wilhelms-Universität Münster, D-48149 Münster, Germany; and [e]Department of Geosciences and Natural Resource Management, University of Copenhagen, DK-1350, Copenhagen, Denmark

Edited by Timothy W. Lyons, University of California, Riverside, CA, and accepted by the Editorial Board June 30, 2015 (received for review February 23, 2015)

The end-Permian mass extinction, the most severe biotic crisis in the Phanerozoic, was accompanied by climate change and expansion of oceanic anoxic zones. The partitioning of sulfur among different exogenic reservoirs by biological and physical processes was of importance for this biodiversity crisis, but the exact role of bioessential sulfur in the mass extinction is still unclear. Here we show that globally increased production of organic matter affected the seawater sulfate sulfur and oxygen isotope signature that has been recorded in carbonate rock spanning the Permian–Triassic boundary. A bifurcating temporal trend is observed for the strata spanning the marine mass extinction with carbonate-associated sulfate sulfur and oxygen isotope excursions toward decreased and increased values, respectively. By coupling these results to a box model, we show that increased marine productivity and successive enhanced microbial sulfate reduction is the most likely scenario to explain these temporal trends. The new data demonstrate that worldwide expansion of euxinic and anoxic zones are symptoms of increased biological carbon recycling in the marine realm initiated by global warming. The spatial distribution of sulfidic water column conditions in shallow seafloor environments is dictated by the severity and geographic patterns of nutrient fluxes and serves as an adequate model to explain the scale of the marine biodiversity crisis. Our results provide evidence that the major biodiversity crises in Earth's history do not necessarily implicate an ocean stripped of (most) life but rather the demise of certain eukaryotic organisms, leading to a decline in species richness.

sulfur cycle | end-Permian mass extinction | primary productivity

The end-Permian mass extinction (EPME) is marked by ∼80% marine biodiversity loss (1). This event is linked with turmoil in the biogeochemical carbon and sulfur cycles (2–4), alongside evidence for abrupt climate change and widespread euxinic (free H_2S) and anoxic water column conditions (5–7). Climate feedback mechanisms might have affected the biogeochemical cycles and may have spawned large-scale adverse conditions detrimental for many organisms (8). Regionally increased primary productivity (9–11) and successive enhanced organic matter degradation by microbial sulfate reduction (MSR), which produces H_2S as a by-product, has been held responsible for euxinic conditions during this time interval (12, 13). Even at a micromolar level, hydrogen sulfide is poisonous for most eukaryotic organisms, as it obstructs mitochondrial energy metabolism (14). The sulfate-reducing prokaryotes that drive this H_2S production are a key catalyst of the biogeochemical sulfur cycle (15) and are associated with a cell-internal reaction pathway connected with kinetic isotope fractionation for both sulfate oxygen and sulfur (16, 17). This biochemical transformation of sulfate linked with an additional oxidative sulfur subcycle, mainly as microbial sulfur disproportionation, and sedimentary sulfide burial can leave a distinct imprint on the isotope composition of the marine sulfate pool (15, 18). In addition, MSR is intimately tied to organic carbon (OC) availability and is the most important contributor to sedimentary OC remineralization on the continental shelf, after aerobic respiration, and thereby fuels the biogeochemical carbon cycle (15, 19, 20). Measuring sulfate sulfur and oxygen isotopes in marine sediments can provide important information about biologically induced sulfur transmissions among different reservoirs (21–23) and can record a global signal (15, 23).

We produced a new high-resolution dataset of carbonate-associated sulfate (CAS) sulfur and CAS oxygen isotopes spanning the time interval of the EPME. Changes in the marine dissolved sulfate isotope composition are considered to be faithfully captured by CAS (4, 15, 23), and chromium-reducible sulfur (CRS) records the products of MSR (15, 24). Carbonate rock was collected at the Kuh-e-Ali Bashi 1 (38.940°N, 45.520°E) and Zal (38.733°N, 45.580°E) sections of the Julfa region (NW Iran, Fig. 1), which were situated on the north-northeastern margin of the NW Iranian Terrane, belonging to the Cimmerian Microcontinent during the latest Permian (ref. 25, Fig. 1). These sections represent an excellent stratigraphic correlation and age assignment (*Timescale* and Figs. S1 and S2). Carbonate rock successions spanning the Permian–Triassic (P–Tr) boundary interval in this area can be divided into two major lithological units: the Ali Bashi Formation made up of the *Paratirolites* Limestone Member marking the upper part and the Zal Member marking the lower part (Fig. S1). The Aras Member (26), or "Boundary Clay," and the following limestone unit, belong to the Elikah Formation (Fig. S1). The Zal Member consists, predominantly, of shales with some intercalations of limestone and marls. The red nodular *Paratirolites* Limestone beds are classified as argillaceous limestone. Macrofossil assemblages consist of rare ammonoids, nautiloids, rugose corals, and brachiopods. This unit is conformably overlain by the Aras Member, which records a marked reduction

Significance

This study provides geochemical evidence that links some of the most important finds associated with the end-Permian mass extinction, including climate warming, enhanced weathering, increased primary productivity, and widespread marine anoxia under a common denominator: the linked biogeochemical sulfur and carbon cycles. Lethal marine conditions are likely the result of climate feedback mechanisms acting to increase nutrient input to the ocean, thereby stimulating global organic carbon production. With future projected climate change in mind, such climate feedback mechanisms could induce widespread eutrophication and expansion of anoxic and sulfidic zones, thereby fundamentally altering marine ecosystems.

Author contributions: M.S., D.K., and C.K. designed research; M.S., A.S., and H.S. performed research; M.S. analyzed data; M.S., A.S., A.G., H.S., D.K., and C.K. wrote the paper; and A.G. performed micropalaeontological analysis.

The authors declare no conflict of interest.

This article is a PNAS Direct Submission. T.W.L. is a guest editor invited by the Editorial Board.

[1]To whom correspondence should be addressed. Email: schobbenmartin@gmail.com.

This article contains supporting information online at www.pnas.org/lookup/suppl/doi:10.1073/pnas.1503755112/-/DCSupplemental.

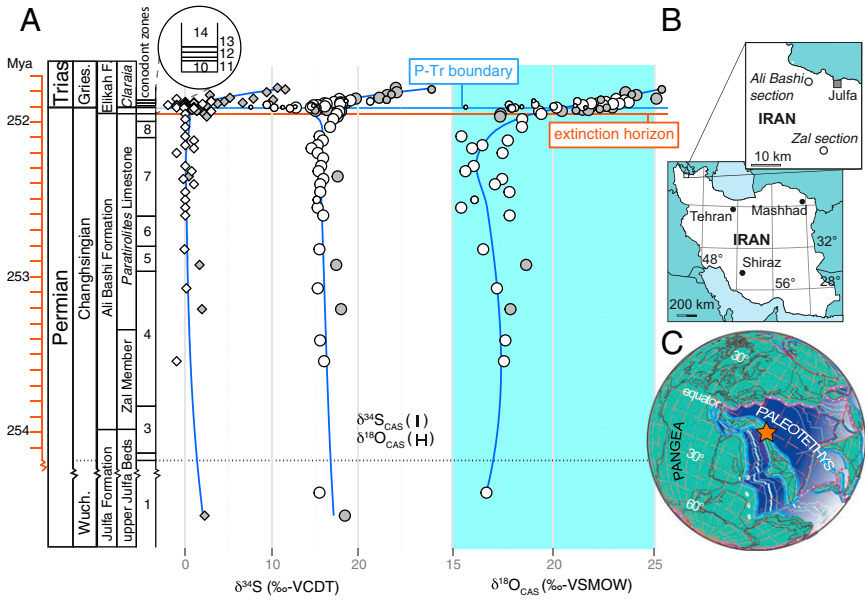

Fig. 1. Stratigraphy and geography. (*A*) Isotopic composition of CAS (circle) and CRS (diamond) of carbonates from Kuh-e-Ali Bashi (white) and Zal (gray). Significant changes in these geochemical records, discernable in the blue lines (loess fit), mark the extinction horizon and suggest a substantial perturbation of the sulfur cycle. Error bars denote reproducibility (2σ; Tables S1 and S2). The temporal framework is constructed by ages for conodont biozones (Figs. S1 and S2 and *Timescale*): 1, *C. Orientalis*; 2, transition; 3, *C. subcarinata*; 4, *C. chanxingensis*; 5, *C. bachmanni*; 6, *C. nodosa*; 7, *C. yini*; 8, *C abadehensis*; 9, *C. hauschkei*; 10, *H. praeparvus-M. ultima*; 11, *H. parvus*; 12, *H. lobota*; 13, *I staeschei*; and 14, *I. isarcica*. The size of individual CAS data points stands for the confidence of representing true seawater chemistry: large, high confidence; small, low confidence (high CRS and non-CAS); medium, intermediate confidence (high CRS or non-CAS; Fig. S3, Tables S3 and S4, and *Reliability of the CAS Proxy*). Geographic location of the sections (*B*) today and (*C*) during the P–Tr (modified from ref. 25).

of $CaCO_3$ (26). In addition, the Permian faunal elements disappear in this unit; therefore the boundary between these units is considered the extinction horizon (ref. 26, Fig. S1). On top of the clay-rich Aras Member, the remainder of the Elikah Formation consists of limestone beds. These lithologies were deposited as a deep-water carbonate platform and did not undergo large-scale sea level changes (*Facies Description*). Therefore, this carbonate platform with an isolated location in the Paleotethys (Fig. 1) bears a large potential for obtaining secular changes of ocean chemistry across the EPME (Fig. 1). Stratigraphic patterns in these CAS sulfur and oxygen isotope records allow for a better understanding of the sulfur cycle across the EPME, thus enabling the assessment of its potential impact on biodiversity.

Results and Discussion

To obtain a primary seawater chemistry signal, samples likely to be contaminated during rock diagenesis by allochtonous sulfur sources, such as leachable sulfate (non-CAS) and sulfide minerals, are identified (*Reliability of the CAS Proxy* and Fig. S3). This enables the construction of the primary stratigraphic CAS oxygen and sulfur isotopic record (Fig. 1). In contrast to previous CAS studies of this time interval (3, 4), the preextinction CAS isotope record (~2 My) is remarkably stable around 17‰ for both $\delta^{34}S_{CAS}$ and $\delta^{18}O_{CAS}$ values with a spread of 1‰ and 2–3‰, respectively (Fig. 1). A ~3‰ negative $\delta^{34}S_{CAS}$ excursion and a 5–7‰ positive shift in $\delta^{18}O_{CAS}$ can be traced for both sites during a ~40 ky period following the marine extinction horizon. A positive $\delta^{34}S_{CAS}$ excursion is found above the conodont-defined P–Tr boundary (~3 m; Fig. S1) with values ~5‰ heavier compared with preextinction strata.

Microbial sulfate reduction is an important aspect in the sulfur cycle, and the associated isotopic fractionation leads to ^{34}S and ^{18}O enrichments of the residual sulfate pool (4, 27). Most of the MSR-produced H_2S will be reoxidized, and only a fraction is buried as sedimentary sulfide serving as a sink for ^{32}S (22); some H_2S can escape the sediment, especially under low O_2 concentrations (8). Hydrogen sulfide release from the sediment is, however, also a factor of sulfide formation and reactive iron availability (8, 22). Continental oxidative weathering and mantle-derived sulfur are fluxes that have a depleted sulfur and oxygen isotopic composition compared with seawater sulfate (4, 24, 27). Evaporite formation and successive burial (with a negligible fractionation) is a sink of sulfate, but its importance depends largely on the extent of suitable environments for deposition [with net evaporation rates (28)]. In contrast to the isotope value of sulfate sulfur, $\delta^{18}O_{SO4}$ is considerably affected by MSR and microbial sulfur disproportionation (29). Sulfur disproportionation produces sulfate with an oxygen isotope fractionation of ~18‰ over the oxygen isotope composition of ambient sea water (29). In contrast to the sulfur isotope part of the sulfur cycle, this microbial-dominated sulfur subcycle is effectively a sink for ^{16}O (4, 29). These different reaction pathways for the sulfur and oxygen ionic compounds of sulfate might lead to a dissimilar temporal evolution of marine sulfate sulfur and oxygen isotope composition, such as recorded by the deviating CAS $\delta^{34}S$ and $\delta^{18}O$ at the extinction horizon in the dataset (Fig. 1).

A depleted sulfate reservoir, in comparison with modern values of 28 mM, has been implied for allowing rapid changes of seawater $\delta^{34}S_{SO4}$ (21), such as observed here for the EPME (>0.1‰·ky^{-1}). The offset in $\delta^{34}S$ between CAS and CRS ($\Delta^{34}S$) was often attributed to the kinetic isotope fractionation of MSR (15). A closed system of diagenetic sedimentary sulfide formation can lead to a small $\Delta^{34}S$ due to ongoing sulfate depletion by MSR (15, 30), whereas a sulfate unlimited system, such as water column pyrite formation (e.g., in the modern Black Sea), can lead to a $\Delta^{34}S$ of 45 ± 15‰ (15, 30, 31). The observed constant $\Delta^{34}S$ (15–16‰) is invariant to burial rate changes (Fig. S2), and might suggest low sulfate levels within sedimentary porewater and the water column (cf. refs. 24 and 30).

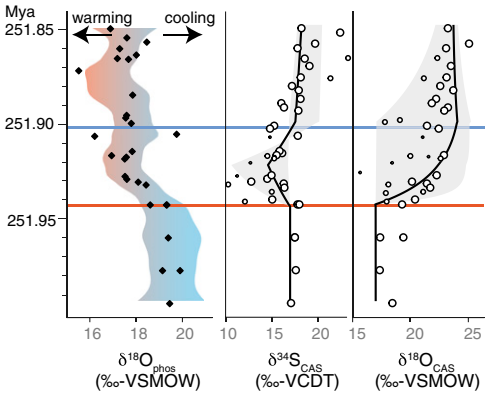

Fig. 2. Isotopic composition of CAS (circle) and numerical solution when perturbing the system with a 16-fold increase in the global weathering flux after the extinction horizon (black line). Gray area represents range of sensitivity experiments (Fig. S4). Time-equivalent seawater temperature rise, seen in $\delta^{18}O_{phos}$ (7), can enforce an enhanced hydrological cycle stimulating larger terrestrial weathering fluxes.

We applied a box model calculation (Methods) to delineate the fluxes that determine the isotopic composition of the marine sulfate across the P–Tr transition. Paleontological and sedimentological evidence from the Iranian sections show no indications of pervasive water column anoxia (*Facies Description*); this is in contrast to the inferred Late Permian marine anoxia at sites in South China and Australia (13, 32). This spatial heterogeneous pattern can be best explained by increased nutrient influx only into parts of the Tethys. This influx caused regional eutrophication associated with increasing extents of oxygen minimum zones (33) and euxinic conditions (12) rather than deep bottom water anoxia caused by a stagnant water column. Widespread ocean fertilization and drawdown of water column O_2 levels have been related to an increased influx of terrestrial material (12, 33) from soil erosion (34) and enhanced weathering (35) initiated by acid precipitation and destabilization of vegetation and soils (34), global warming, and an associated intensified hydrological cycle at that time (7). The climax of this biogeochemical cascade correlates with the greenhouse warming often associated with coeval Siberian Trap volcanism (2, 5). The importance of organic substrates for MSR justifies the incorporation of the OC pool and the link to continental weathering in our box model. This simplified approach is further justified because the continental supply of nutrients fertilizes the oceanic shelf connected with highest MSR activity and OC decomposition rates, which are almost equal in oxic and euxinic sediments (19, 20).

A best model fit, based on sensitivity experiments (*Sensitivity Experiments* and Fig. S4), suggests a 16-fold increase in the weathering flux that stimulates a >16-fold global marine OC inventory, starting at the extinction horizon and lasting for a period of 40 ky (Fig. 2). This stimulates large MSR activity (>17-fold) but also sulfur disproportionation (Methods), although it has been suggested that the latter could not explain an oxygen isotope fractionation of >18‰ between water and sulfate (29). An average $\delta^{18}O_{seawater}$ of ~−1‰ (6) and $\delta^{18}O_{CAS}$ excursion to values of >20‰ make sulfur disproportionation an unlikely candidate. Increased OC degradation by MSR is a strong and robust argument for the reconstructed scenario and explains the observed $\delta^{18}O_{CAS}$ excursion. Independent numerical exercises with higher complexity models suggest that >4 times enhanced continental weathering considerably increases the primary productivity in shelf settings (12, 36), followed by anoxic and sulfidic conditions as a consequence of increased (an)aerobic OC remineralization.

The initial negative $\delta^{34}S_{CAS}$ excursion also suggests that pyrite burial did not increase with enhanced MSR activity, as is often assumed (4, 27). The main controlling factors for pyrite formation are labile OC, sulfide formation, oxygenation conditions, and highly reactive iron [$Fe_{(HR)}$] availability in the sediment and water column (22). In sulfidic water column conditions, such as the modern Black Sea, which represents only a fraction of the total modern ocean volume (27), pyrite formation is a syngenetic process (Fig. 3) rather than a diagenetic process (31, 37). This pyrite sedimentation style depletes $Fe_{(HR)}$ already in the water column and largely inhibits the pyrite formation within the sediment (31). In such euxinic settings, pyrite formation becomes iron-limited and pyrite burial becomes sensitive to the supply of $Fe_{(HR)}$ to the ocean (38). Mechanisms for $Fe_{(HR)}$ supply are hydrothermal input, windblown dust, riverine input, and diagenetic iron cycling on the shelf (39, 40). Although the iron flux from the continent is potentially large, 70–90% of the $Fe_{(HR)}$ is already lost as

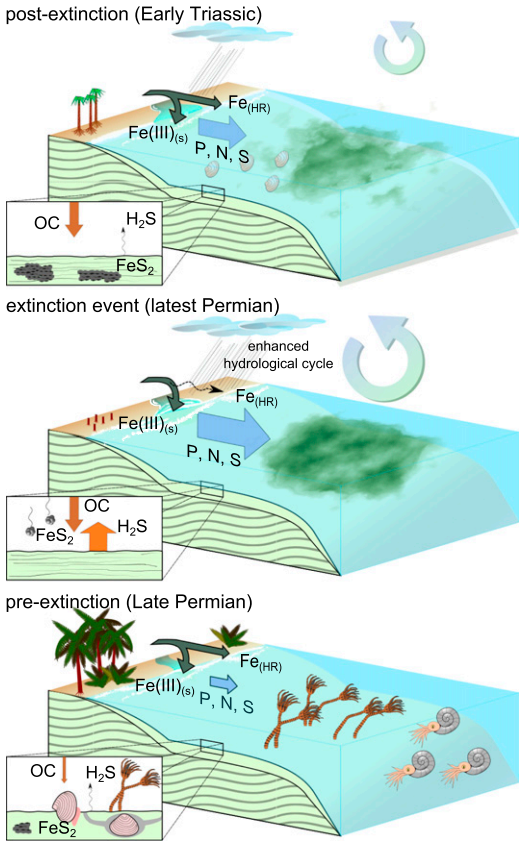

Fig. 3. Conceptual model for environmental changes across the P–Tr boundary, depicting the shelf settings that are prone to be affected in a scenario of intensified continental influx. Preextinction Late Permian marine communities would consist of multiple trophic levels. Authigenic pyrite formation is supported by sulfide production during anaerobic OC remineralization via MSR and nonlimiting iron availability. The extinction event marks an increased terrigenous influx causing local eutrophication as well as the input of isotopically depleted sulfur, aided by an intensified hydrological cycle forced by global warming. Increased sediment load and turbulence of river discharge flocculates iron as Fe oxy(hydr)oxides in estuaries, reducing the ocean $Fe_{(HR)}$ inventory. Consequential OC remineralization by MSR and $Fe_{(HR)}$ limitation raises seawater H_2S. Sulfide toxicity alongside marine anoxia sustains a low-species richness but a high-biomass marine community. Pyrite sedimentation is limited to small amounts of syngenetic pyrite precipitation. Relaxation of physical continental weathering reduces ocean input of nutrients and raises $Fe_{(HR)}$ delivery to the postextinction ocean, thereby reducing sulfidic water column conditions and relocating pyrite sedimentation toward the sediments, where decreased O_2 irrigation due to a less active benthic community stimulates authigenic pyrite formation. The enlarged OC pool is sustained due to carbon recycling by an active microbial community.

particles in estuaries (40). The iron reaching the ocean is sensitive to water turbulence and grain concentrations delivered by rivers (40). Relating all this to the end-Permian scenario, a situation under a high sea level (5) and a sudden influx of soils (34) accompanied by high physical erosion rates (35) due to an intensified hydrological cycle in a warmer ocean (7) would create an environment that already depletes $Fe_{(HR)}$ before entering the ocean (Fig. 3).

We do not provide an estimate for the pyrite flux change. However, under the Late Permian oceanic conditions, it was not necessary that pyrite burial increased concomitantly with increasing MSR. The diverging CAS sulfur and oxygen isotope pattern can be best explained by increased levels of MSR but decreased pyrite burial, compatible with an enlarged global extent of iron-limited euxinic seawater (Figs. 2 and 3). The presence of green sulfur bacteria—which thrive in H_2S-rich surface water—during the time interval of the sulfur cycle perturbation, evidenced by biomarker analyses (32), suggests widespread euxinia. Moreover, ocean fertilization is in concert with an independent model for the Late Permian ocean, suggesting 10 times higher nutrient levels to induce globally pervasive water column H_2S (12). The new CAS isotope data and the related environmental conditions suggest that the euxinic zones expanded suddenly at the extinction horizon (Fig. 3). Synchronicity of the two observations support the notion that sulfidic toxicity drove the marine biodiversity loss at the EPME, as first hypothesized by Kump et al. (8). However, the entire continental shelf area [$\sim 5.8e^6$ km^2 for the latest Permian (28)] would be primarily affected in our conceptual model, in contrast to only upwelling regions with a comparatively smaller total dimension [$\sim 0.4e^6$ km^2 for the modern ocean (8)]. Predominant sulfate reduction on the shelf, rather than in the deep sea, agrees with observations in the modern ocean of decreasing MSR with increasing distance to land (19, 22). In addition, a marine region would be targeted that is the locus of Paleozoic biological activity (the neritic realm), and thereby this conceptual model fulfills all criteria as suggested by Wignall and Twitchett (5) to explain a wholesale collapse of marine invertebrate diversity. However, the geography and nutrient load of weathering fluxes would also be an important determinant of the spatial distribution and severity of productivity-driven redox changes (oxic, nonsulfidic anoxic, and euxinic) (41). Regionally biased ecosystem destruction would leave refugia with less adverse conditions and would allow rapid recolonization of vacant ecospaces through migration of survivors. Postextinction species are frequently found to occur along a spectrum of environments, and within-habitat diversity is typically higher than diversity between habitats, a pattern explained by species that exploit the full range of the available niches under low competition pressure (42). Also, refilling of vacant ecospace by an ecologically diverse group of survivors can explain why, on a global scale, ecosystems remained operating even though species diversity collapsed (43).

This scenario to explain the EPME enhances the notion that life can influence seawater chemistry (22) and the relationship to OC remineralization (13). CAS isotopes provide a more direct view on biological productivity in past oceans, suggesting a flourishing of life. It is in stark contrast with the concept of decreased OC production, or "Strangelove" ocean, often implied in extinction scenarios (44). This study also emphasizes that, besides the property of organisms to construct a habitable planet (21), they can also act as a catalyst for destruction. However, marine life might have been very different with mainly prokaryotes dominating over eukaryotes (11, 45). A return to nearly preextinction $\delta^{34}S_{CAS}$, within 40 ky, suggests recommencing pyrite burial; the disturbance was therefore a rather transient event, which agrees with the postulated short duration of soil erosion and local euxinic surface water conditions (32, 34). It argues for an enhanced supply of iron, possibly under reduced detrital loading of river discharge, a waning of the global extent of euxinic conditions and consequential increase of diagenetic pyrite accumulation, or a combination of both (Fig. 3).

The subsequent Early Triassic positive $\delta^{34}S_{CAS}$ is apparently not directly related to the biodiversity crisis (Fig. 1). Rather it records increased sequestration of sulfur by authigenic pyrite caused by the lack of organisms that normally irrigated sediments with O_2 by burrowing (22) (Fig. 3). Reduced sediment mixing has been documented by the decreased thickness of the sedimentary mixed layer and the absence of burrowing faunas at localities globally, a possible symptom of the widespread devastation (5, 46). The relatively stable and high $\delta^{18}O_{CAS}$ in this period indicates that MSR remained important during the Early Triassic. Persisting high levels of MSR suggests a prevailing large OC pool, together with a long-lasting (~800 ky) increase in continental weathering (35), a perturbed carbon cycle, and high global temperatures, the latter two returning in intervals throughout a period of almost 4 My (47, 48). These Earth surface processes are regarded as an important negative feedback loop of the carbon cycle, where enhanced production and sequestration of OC is stimulated by global warming and subsequent chemical weathering rates (36). The prolonged disturbance after the EPME contradicts a fast return (<100 ky) to predisturbance climate and carbon cycle, enforced by carbon sequestration, as suggested for other events marked by greenhouse warming, such as the Cenozoic hyperthermals (49). Degradation of organic substrates on the seafloor by sulfate-reducing microbes, possibly in conjunction with more-efficient water column carbon cycling of labile bacterial OC (45) and low fecal pellet production by reduced numbers of zooplankton (10), might all facilitate a sustained large marine OC pool. The postextinction prokaryote-dominated marine communities, in particular sulfate-reducing microbes, might therefore have had a crucial control on the Early Triassic carbon cycle and would affect marine redox conditions and climate with an adverse effect on the biotic recovery.

Methods

The applied CAS extraction method minimizes the potential alteration of the CAS sulfur or oxygen isotope signal during the analytical procedure by the use of subsequent NaCl leaches (50). The NaCl leaches are precipitated with a $BaCl_2$ solution, and, subsequently, the concentration of the sulfate fraction not structurally substituted within the $CaCO_3$ lattice, leachable non-CAS, is determined gravimetrically. These steps are repeated until no leachable non-CAS is observed. In follow-up, acid digestion of the sample is performed with 25% HCl under restricted atmospheric exchange and in a time window generally not more than 3 h to prevent oxidation of sulfide species. The sulfate of the digested carbonate rock is also precipitated as barium sulfate, and CAS concentrations are gravimetrically determined.

The sulfur isotopic composition of the leachable non-CAS and CAS (Fig. S3) was obtained by an Elemental Analyzer (EA) connected to a ThermoFinnigan Delta Plus mass spectrometer and is reported in the standard ($\delta^{34}S$) notation relative to Vienna Cañon Diablo Troilite (VCDT) in per mil. Precision was confirmed by repeated measurements on the international standards and internal laboratory standards. This yielded an accuracy of 0.09‰ and a reproducibility on average better than 0.40‰ (Table S1). The oxygen isotopic composition of the leachable non-CAS and CAS was measured with a high temperature conversion/EA interfaced to a ThermoFinnigan Delta Plus XL mass spectrometer and is reported in the standard ($\delta^{18}O$) notation relative to Vienna Standard Mean Ocean Water (VSMOW) in per mil. International standards and an in-house standard were used to determine the precision of the procedure. This resulted in an accuracy of 0.40‰ and a reproducibility of ±0.80‰ (Table S2).

The CRS content was extracted from the remaining residue after the CAS extraction by the chromium reduction method (51). Under continuous N_2 flow, samples were reacted with HCl and chromium powder to produce acidic chromium chloride and were heated to a gentle boil for 1.5 h. Sulfur was trapped as zinc sulfide in a zinc acetate solution and converted to silver sulfide for filtrating and drying. The CRS concentrations of the residues were determined gravimetrically. For sulfur isotopic analyses ($\delta^{34}S$), extracted silver sulfide was weighed into tin capsules withV_2O_5 added to aid in combustion. Isotope measurements were performed on a Costech Elemental Combustion System 4010 connected to a Thermo Delta V+ Isotope Ratio mass spectrometer with results reported relative to VCDT in per mil. Precision was confirmed by

repeated measurements on the international standards [International Atomic Energy Agency (IAEA)-S-1, IAEA-S-2, IAEA-S-3, National Bureau of Standards (NBS)-127] and resulted in an accuracy of 0.24‰ and a reproducibility on average better than 0.40‰.

A box model was constructed, to delineate which fluxes could be responsible for isotopic changes in marine sulfate and thus could explain the stratigraphic CAS isotope record. Sulfate mass (M_{SO4}) and isotopic composition (δ_{SO4}) are estimated with the following equations, adapted from ref. 24:

$$\frac{dM_{SO4}}{dt} = Q_w + Q_v + Q_m - (F_p + F_e) \quad [1]$$

$$\frac{d\delta_{SO4}}{dt} = \frac{Q_w\delta_w + Q_v\delta_v + Q_m\delta_m - \delta_{SO4}(Q_w + Q_v + Q_m) - F_p\Delta_{MSR}}{M_{SO4}} \quad [2]$$

where Q_w represents the weathering input flux, δ_w is the isotopic composition of weathering input, Q_v is the volcanic input flux, δ_v is the isotopic composition of volcanic input, Q_m is the hydrothermal input flux, δ_m is the isotopic composition of the hydrothermal input flux, F_e is the evaporite burial flux, F_p is the pyrite burial flux, and Δ_{MSR} is the average isotopic fractionation associated with MSR. The oxygen and sulfur isotopic compositions of marine sulfate are affected by different processes. Two aspects are mainly responsible for this difference, microbial sulfur cycling and the exchange and cycling through the oceanic crust. Microbial sulfur cycling results in the loss of oxygen during MSR (F_{MSR}), whereas the product (sulfide) is oxidized and mainly via microbial sulfur disproportionation (29) transformed back to sulfate, Q_{ox}, both with an effect on the isotopic composition. The surplus of these bacterial processes will be buried as sedimentary sulfide, mainly pyrite, and can be envisioned as

$$F_p = F_{MSR} - Q_{ox}, \quad [3]$$

whereas marine sulfate $\delta^{34}S$ is only affected by hydrothermal S input in one direction, sulfate $\delta^{18}O$ is modified by oxidation of sulfides at these hydrothermal vents (Q_h) and acquires a $\delta^{18}O$ similar to ocean water (29). On the other hand, anhydrite formation in the oceanic crust is an effective sink for sulfate oxygen (F_s), without fractionation (29) and can be described by

$$Q_m = Q_h - F_s. \quad [4]$$

To adjust for these differences imposed upon the marine sulfate $\delta^{18}O$, Eqs. **3** and **4**, are substituted into Eq. **1**, yielding

$$\frac{d\delta_{SO_4}}{dt} = \frac{Q_w\delta_w + Q_v\delta_v + Q_h\delta_m + Q_{ox}\delta_{ox} - \delta_{SO4}(Q_w + Q_v + Q_h + Q_{ox}) - F_{MSR}\Delta_{MSR}}{M_{SO4}} \quad [5]$$

where δ_{ox} stands for the isotopic composition of sulfate originating from sulfur disproportionation. Steady state was achieved by modifying Holocene reservoir and flux size and isotopic composition, to approximate the sulfur cycle of the P–Tr interval (*Steady-State Sulfur Cycle Model* and Table S5). To exploit the important impact of MSR on OC remineralization (19), an OC pool (M_{OC}) was introduced to the model, by linking Q_w linearly to ocean primary productivity (Q_{po}). OC burial (F_{bo}) and OC remineralization (F_{OC}) are determined by the size of the OC pool as first-order removal constants (k values); k values are determined by assuming that 99% of OC is remineralized of which part is remineralized by MSR (F_{MSR}; Table S5), and according to the stoichiometry of the two biochemical reactions

$$CH_2O + O_2 \Leftrightarrow CO_2 + H_2O \quad [6]$$

$$2CH_2O + SO_4 \Leftrightarrow 2HCO_3 + H_2S. \quad [7]$$

The size of the marine OC pool is described by

$$M_{OC(t)} = \left[\left(\frac{Q_{po(i)}}{k1+k2}\right) - \left[\left(\frac{Q_{po(i)}}{k1+k2}\right) - M_{OC(i)}\right] e^{(-(k1+k2)t)}\right] - 2F_{MSR} \quad [8]$$

where (i) stands for the initial pool and (t) stands for the pool changing with time. The relation between the OC pool and MSR is described in the following equation, taken from ref. 22:

$$F_{MSR} = \alpha M_{OC}[SO_4]^y, \quad [9]$$

which considers that the size of the OC pool has a direct impact on the availability of OC for sulfate reduction. Factor α is calculated by solving the equation with the initial values, and y has been taken as 0.3, in accordance with ref. 22. The model was perturbed by varying the weathering flux concomitant with the extinction horizon for a duration of 40 ky. Various simulations were performed, with the weathering flux changing from 2 to 64 times larger than the background value. The Triassic weathering flux is taken to be 7 times higher than the Permian (35). To simulate the effect of a largely iron-limited euxinic ocean, the fraction of pyrite buried was set to 10 times reduced for 20 ky following the extinction horizon, followed by a twofold increase for another 20 ky compared with the preperturbed value.

ACKNOWLEDGMENTS. The Aras Free Zone office and Adel Najafzadeh are thanked for permission to sample the locations in the Julfa region (NW Iran). We furthermore thank the following persons for technical assistance; Robert Schreiber, Melanie Rühl, Kathrin Krahn, and Artur Fugmann. Acknowledgments are also due to Robyn Hannigan and Sonny A. Walton for comments on the manuscript. R.H. is thanked for access to the Environmental Analytical Facility at the University of Massachusetts Boston [National Science Foundation (NSF) Award 09-42371 DBI, R.H. and Alan Christian]. This project was funded by the Deutsche Forschungsgemeinschaft (Projects KO2011/8-1 and KO1829/12-2 provided to C.K. and D.K.) and the NSF Graduate Research Fellowship Program (Grant DGE-1356104).

1. Alroy J, et al. (2008) Phanerozoic trends in the global diversity of marine invertebrates. *Science* 321(5885):97–100.
2. Erwin DH (1994) The Permo-Triassic extinction. *Nature* 367(6460):231–236.
3. Riccardi AL, Arthur MA, Kump LR (2006) Sulfur isotopic evidence for chemocline upward excursions during the end-Permian mass extinction. *Geochim Cosmochim Acta* 70(23):5740–5752.
4. Newton RJ, Pevitt EL, Wignall PB, Bottrell SH (2004) Large shifts in the isotopic composition of seawater sulphate across the Permo–Triassic boundary in northern Italy. *Earth Planet Sci Lett* 218(3-4):331–345.
5. Wignall PB, Twitchett RJ (1996) Oceanic anoxia and the end Permian mass extinction. *Science* 272(5265):1155–1158.
6. Joachimski MM, et al. (2012) Climate warming in the latest Permian and the Permian–Triassic mass extinction. *Geology* 40(3):195–198.
7. Schobben M, Joachimski MM, Korn D, Leda L, Korte C (2014) Palaeotethys seawater temperature rise and an intensified hydrological cycle following the end-Permian mass extinction. *Gondwana Res* 26(2):675–683.
8. Kump LR, Pavlov A, Arthur MA (2005) Massive release of hydrogen sulfide to the surface ocean and atmosphere during intervals of oceanic anoxia. *Geology* 33(5):397–400.
9. Algeo T, et al. (2012) Evidence for a diachronous Late Permian marine crisis from the Canadian Arctic region. *Geol Soc Am Bull* 124(9-10):1424–1448.
10. Algeo TJ, et al. (2010) Changes in productivity and redox conditions in the Panthalassic Ocean during the latest Permian. *Geology* 38(2):187–190.
11. Algeo TJ, et al. (2013) Plankton and productivity during the Permian–Triassic boundary crisis: An analysis of organic carbon fluxes. *Global Planet Change* 105(0):52–67.
12. Meyer KM, Kump LR, Ridgwell A (2008) Biogeochemical controls on photic-zone euxinia during the end-Permian mass extinction. *Geology* 36(9):747–750.
13. Brennecka GA, Herrmann AD, Algeo TJ, Anbar AD (2011) Rapid expansion of oceanic anoxia immediately before the end-Permian mass extinction. *Proc Natl Acad Sci USA* 108(43):17631–17634.
14. Knoll AH, Bambach RK, Payne JL, Pruss S, Fischer WW (2007) Paleophysiology and end-Permian mass extinction. *Earth Planet Sci Lett* 256(3-4):295–313.
15. Strauss H (1999) Geological evolution from isotope proxy signals—Sulfur. *Chem Geol* 161(1-3):89–101.
16. Sim MS, Bosak T, Ono S (2011) Large sulfur isotope fractionation does not require disproportionation. *Science* 333(6038):74–77.
17. Mandernack KW, Krouse HR, Skei JM (2003) A stable sulfur and oxygen isotopic investigation of sulfur cycling in an anoxic marine basin, Framvaren Fjord, Norway. *Chem Geol* 195(1-4):181–200.
18. Johnston DT, et al. (2005) Active microbial sulfur disproportionation in the Mesoproterozoic. *Science* 310(5753):1477–1479.
19. Jørgensen BB (1982) Mineralization of organic matter in the sea bed—The role of sulphate reduction. *Nature* 296(5858):643–645.
20. Canfield DE (1989) Sulfate reduction and oxic respiration in marine sediments: Implications for organic carbon preservation in euxinic environments. *Deep Sea Res A* 36(1):121–138.
21. Kah LC, Lyons TW, Frank TD (2004) Low marine sulphate and protracted oxygenation of the Proterozoic biosphere. *Nature* 431(7010):834–838.
22. Canfield DE, Farquhar J (2009) Animal evolution, bioturbation, and the sulfate concentration of the oceans. *Proc Natl Acad Sci USA* 106(20):8123–8127.
23. Goldberg T, Poulton SW, Strauss H (2005) Sulphur and oxygen isotope signatures of late Neoproterozoic to early Cambrian sulphate, Yangtze Platform, China: Diagenetic constraints and seawater evolution. *Precambrian Res* 137(3-4):223–241.
24. Adams DD, Hurtgen MT, Sageman BB (2010) Volcanic triggering of a biogeochemical cascade during Oceanic Anoxic Event 2. *Nat Geosci* 3(3):201–204.
25. Stampfli GM, Borel GD (2002) A plate tectonic model for the Paleozoic and Mesozoic constrained by dynamic plate boundaries and restored synthetic oceanic isochrons. *Earth Planet Sci Lett* 196(1-2):17–33.

26. Ghaderi A, Leda L, Schobben M, Korn D, Ashouri AR (2014) High-resolution stratigraphy of the Changhsingian (Late Permian) successions of NW Iran and the Transcaucasus based on lithological features, conodonts and ammonoids. *Fossil Rec* 17(1):41–57.
27. Owens JD, et al. (2013) Sulfur isotopes track the global extent and dynamics of euxinia during Cretaceous Oceanic Anoxic Event 2. *Proc Natl Acad Sci USA* 110(46): 18407–18412.
28. Halevy I, Peters SE, Fischer WW (2012) Sulfate burial constraints on the Phanerozoic sulfur cycle. *Science* 337(6092):331–334.
29. Turchyn AV, Schrag DP (2004) Oxygen isotope constraints on the sulfur cycle over the past 10 million years. *Science* 303(5666):2004–2007.
30. Song H, et al. (2014) Early Triassic seawater sulfate drawdown. *Geochim Cosmochim Acta* 128(0):95–113.
31. Wilkin RT, Arthur MA (2001) Variations in pyrite texture, sulfur isotope composition, and iron systematics in the Black Sea: Evidence for Late Pleistocene to Holocene excursions of the O_2-H_2S redox transition. *Geochim Cosmochim Acta* 65(9):1399–1416.
32. Grice K, et al. (2005) Photic zone euxinia during the Permian-triassic superanoxic event. *Science* 307(5710):706–709.
33. Winguth C, Winguth AME (2012) Simulating Permian–Triassic oceanic anoxia distribution: Implications for species extinction and recovery. *Geology* 40(2):127–130.
34. Sephton MA, et al. (2005) Catastrophic soil erosion during the end-Permian biotic crisis. *Geology* 33(12):941–944.
35. Algeo TJ, Twitchett RJ (2010) Anomalous Early Triassic sediment fluxes due to elevated weathering rates and their biological consequences. *Geology* 38(11):1023–1026.
36. Ozaki K, Tajima S, Tajika E (2011) Conditions required for oceanic anoxia/euxinia: Constraints from a one-dimensional ocean biogeochemical cycle model. *Earth Planet Sci Lett* 304(1-2):270–279.
37. Lyons TW, Berner RA (1992) Carbon-sulfur-iron systematics of the uppermost deepwater sediments of the Black Sea. *Chem Geol* 99(1-3):1–27.
38. Poulton SW, Canfield DE (2011) Ferruginous conditions: A dominant feature of the ocean through Earth's history. *Elements (Quebec)* 7(2):107–112.
39. Lyons TW, Severmann S (2006) A critical look at iron paleoredox proxies: New insights from modern euxinic marine basins. *Geochim Cosmochim Acta* 70(23):5698–5722.
40. Raiswell R (2011) Iron transport from the continents to the open ocean: The aging–rejuvenation cycle. *Elements (Quebec)* 7(2):101–106.
41. Algeo TJ, et al. (2011) Spatial variation in sediment fluxes, redox conditions, and productivity in the Permian–Triassic Panthalassic Ocean. *Palaeogeogr Palaeoclimatol Palaeoecol* 308(1–2):65–83.
42. Hofmann R, et al. (2014) Recovery of benthic marine communities from the end-Permian mass extinction at the low latitudes of eastern Panthalassa. *Palaeontology* 57(3):547–589.
43. Foster WJ, Twitchett RJ (2014) Functional diversity of marine ecosystems after the Late Permian mass extinction event. *Nat Geosci* 7(3):233–238.
44. Rampino MR, Caldeira K (2005) Major perturbation of ocean chemistry and a 'Strangelove Ocean' after the end-Permian mass extinction. *Terra Nova* 17(6): 554–559.
45. Luo G, et al. (2014) Vertical $\delta^{13}C_{org}$ gradients record changes in planktonic microbial community composition during the end-Permian mass extinction. *Palaeogeogr Palaeoclimatol Palaeoecol* 396:119–131.
46. Hofmann R, Buatois LA, MacNaughton RB, Mángano MG (2015) Loss of the sedimentary mixed layer as a result of the end-Permian extinction. *Palaeogeogr Palaeoclimatol Palaeoecol* 428:1–11.
47. Payne JL, et al. (2004) Large perturbations of the carbon cycle during recovery from the end-permian extinction. *Science* 305(5683):506–509.
48. Sun Y, et al. (2012) Lethally hot temperatures during the Early Triassic greenhouse. *Science* 338(6105):366–370.
49. Bains S, Norris RD, Corfield RM, Faul KL (2000) Termination of global warmth at the Palaeocene/Eocene boundary through productivity feedback. *Nature* 407(6801): 171–174.
50. Wotte T, Shields-Zhou GA, Strauss H (2012) Carbonate-associated sulfate: Experimental comparisons of common extraction methods and recommendations toward a standard analytical protocol. *Chem Geol* 326-327:132–144.
51. Canfield DE, Raiswell R, Westrich JT, Reaves CM, Berner RA (1986) The use of chromium reduction in the analysis of reduced inorganic sulfur in sediments and shales. *Chem Geol* 54(1-2):149–155.
52. Richoz S, et al. (2010) Permian–Triassic boundary interval in the Middle East (Iran and N. Oman): Progressive environmental change from detailed carbonate carbon isotope marine curve and sedimentary evolution. *J Asian Earth Sci* 39(4):236–253.
53. Aghai PM, Vachard D, Krainer K (2009) Transported foraminifera in Palaeozoic deep red nodular limestones exemplified by latest Permian Neoendothyra in the Zal section (Julfa area, NW Iran). *Rev Esp Micropalaontol* 41(1-2):197–213.
54. Leda L, et al. (2014) Lithostratigraphy and carbonate microfacies across the Permian–Triassic boundary near Julfa (NW Iran) and in the Baghuk Mountains (Central Iran). *Facies* 59(2):1–31.
55. Kozur HW (2007) Biostratigraphy and event stratigraphy in Iran around the Permian–Triassic Boundary (PTB): Implications for the causes of the PTB biotic crisis. *Global Planet Change* 55(1-3):155–176.
56. Shen SZ, et al. (2011) Calibrating the end-Permian mass extinction. *Science* 334(6061): 1367–1372.
57. Burgess SD, Bowring S, Shen SZ (2014) High-precision timeline for Earth's most severe extinction. *Proc Natl Acad Sci USA* 111(9):3316–3321.
58. Yuan D-x, et al. (2014) Revised conodont-based integrated high-resolution timescale for the Changhsingian Stage and end-Permian extinction interval at the Meishan sections, South China. *Lithos* 204:220–245.
59. Rennie VCF, Turchyn AV (2014) The preservation of and in carbonate-associated sulfate during marine diagenesis: A 25 Myr test case using marine sediments. *Earth Planet Sci Lett* 395:13–23.
60. Lyons TW, Walter LM, Gellatly AM, Martini AM, Blake RE (2004) Sites of anomalous organic remineralization in the carbonate sediments of South Florida, USA: The sulfur cycle and carbonate-associated sulfate. *Spec Pap Geol Soc Am* 379:161–176.
61. Paytan A, Kastner M, Campbell D, Thiemens MH (2004) Seawater sulfur isotope fluctuations in the Cretaceous. *Science* 304(5677):1663–1665.
62. Berner RA, Canfield DE (1989) A new model for atmospheric oxygen over Phanerozoic time. *Am J Sci* 289(4):333–361.
63. Arthur MA (2000) Volcanic contributions to the carbon and sulfur geochemical cycle and global change. *Encyclopedia of Volcanoes*, eds Sigurdsson H, Houghton B, McNutt SR, Rymer H, Stix J (Academic Press, San Diego), pp 1045–1056.
64. Horita J, Zimmermann H, Holland HD (2002) Chemical evolution of seawater during the Phanerozoic: Implications from the record of marine evaporites. *Geochim Cosmochim Acta* 66(21):3733–3756.
65. Black BA, Elkins-Tanton LT, Rowe MC, Peate IU (2012) Magnitude and consequences of volatile release from the Siberian Traps. *Earth Planet Sci Lett* 317-318:363–373.
66. Ripley EM, Lightfoot PC, Li C, Elswick ER (2003) Sulfur isotopic studies of continental flood basalts in the Noril'sk region: Implications for the association between lavas and ore-bearing intrusions. *Geochim Cosmochim Acta* 67(15):2805–2817.
67. Reichow MK, et al. (2009) The timing and extent of the eruption of the Siberian Traps large igneous province: Implications for the end-Permian environmental crisis. *Earth Planet Sci Lett* 277(1-2):9–20.
68. Llyod RM (1967) Oxygen-18 composition of oceanic sulfate. *Science* 156(3779): 1228–1231.
69. RCoreTeam (2014) *R: A Language and Environment for Statistical Computing* (R Found Stat Comput, Vienna).
70. Wickham H (2009) *ggplot2: Elegant Graphics for Data Analysis* (Springer, New York).
71. Ghaderi A (2014) Stratigraphy and paleoecology of the Upper Permian to Permian–Triassic boundary of the Northwest of Iran based on biostratigraphic data of conodonts and brachiopods. PhD thesis (Ferdowsi University of Mashhad, Mashhad, Iran).